Published in final edited form as:
Yan, R., Heil, T., Presser, V., Walczak, R., Antonietti, M., & Oschatz, M. (n.d.). Ordered Mesoporous Carbons with high Micropore Content and Tunable Structure Prepared by Combined Hard- and Salt-Templating as Electrode Materials in Electric Double-Layer Capacitors. *Advanced Sustainable Systems, 2(2): 1700128.* *doi:10.1002/adsu.201700128.*

Ordered Mesoporous Carbons with high Micropore Content and Tunable Structure Prepared by Combined Hard- and Salt-Templating as Electrode Materials in Electric Double-Layer Capacitors

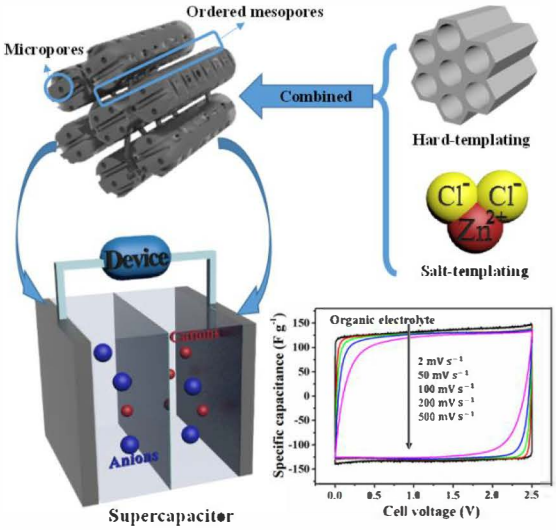

Old order in new supercapacitor electrodes. Combined hard- and salt-templating is used for the synthesis of hierarchical carbon materials with combined ordered mesoporous and micropores. The porosity in both pore systems can be tuned over a wide range and the materials offer high ion storage capacity and outstanding capacity retention at high current density in electric double-layer capacitors with different electrolytes. A microporous shell surrounding the individual particles leads to lower internal resistance of the electrodes.

Ordered Mesoporous Carbons with high Micropore Content and Tunable Structure Prepared by Combined Hard- and Salt-Templating as Electrode Materials in Electric Double-Layer Capacitors

*Runyu Yan, Tobias Heil, Volker Presser, Ralf Walczak, Markus Antonietti, and Martin Oschatz**

R. Yan, Dr. T. Heil, R. Walczak, Prof. Dr. Dr. M. Antonietti, Dr. M. Oschatz
Max Planck Institute of Colloids and Interfaces
Department of Colloid Chemistry
Am Mühlenberg 1, 14476 Potsdam
Germany
E-mail: martin.oschatz@mpikg.mpg.de

Prof. Dr. V. Presser
INM – Leibniz Institute for New Materials & Saarland University
Campus D2 2, 66123 Saarbrücken
Germany

Keywords: porous carbon materials, hierarchical structure, salt-templating, hard-templating, electric double-layer capacitors

Synthesis of high surface area carbon materials with hierarchical pore structure is reported. Combined salt-templating with $ZnCl_2$ and hard-templating with SBA-15 is used to produce ordered mesoporous and microporous hard-salt-templated carbons (OM-HSTCs) from simple sucrose as carbon precursor. OM-HSTCs achieve specific surface areas of more than 2600 $m^2\ g^{-1}$ and total pore volumes up to 2.2 $cm^3\ g^{-1}$. In comparison to purely hard-templated ordered mesoporous carbons, the additional salt-template leads to high micropore volume and provides control over the size/distribution of micro- and mesopores and over the carbon microstructure. This method combines carbonization and the formation of well-defined micropores in one step and is more versatile in terms of resulting pore structure than previously reported routes towards ordered mesoporous/microporous carbons. When applied as electrode materials in electric double-layer capacitors with 1 M tetraethylammonium tetrafluoroborate in acetonitrile organic electrolyte, OM-HSTCs combine high gravimetric

capacitance (133 F g^{-1} at 0.1 A g^{-1}) resulting from high micropore volume with high capacitance retention under high power conditions (126 F g^{-1} at 40 A g^{-1}), exceeding the purely microporous or purely ordered mesoporous reference materials.

1. Introduction

Owing to the increasing electrification of the world, there is an ever-growing demand for the high-performance, cost-effective, and environmentally-friendly electrochemical energy storage systems.[1] Electric double-layer capacitors (EDLCs) have attracted considerable attention in recent years due to their high specific power, long cycle life, and ability to bridge the power/energy gap between conventional capacitors (high power but low energy) and batteries/fuel cells (high energy but low power).[2] In contrast to batteries and battery-like systems based on chemical conversions, charge storage in EDLCs is achieved by electrosorption of electrolyte ions on the surface of charged electrode materials and comparable physicochemical processes, such as changes in solvation and solvent structure. Such devices do not depend on potentially time-consuming redox-reactions and are thus attractive for applications with short time constants (usually in the order of 10^{-2}-10^{2} s)[3] for charge-discharge (e.g., brake energy recovery in cars or recovery of the lift energy in cranes).[4] EDLCs stand out by long cycle life[2b] and a broad range of operating temperatures.[5] However, in most cases the inferior energy density of EDLCs[6] (lower than 10 Wh kg^{-1} for commercial devices) is a significant drawback for their commercial application. It remains an enormous challenge to promote the energy density of EDLCs without sacrificing their most valuable characteristics, the distinguished power density and superior cycling stability. Insights into the fundamentals of the charge storage mechanisms with novel characterization techniques and advanced design of electrode materials are needed to enable high energy EDLCs.[7] These two fields of research often go hand in hand, that is,

fundamental investigations are often more straightforward if well-defined model substances are utilized for such experiments.[7c, 7e]

Nanoporous carbons are highly attractive electrode materials for EDLCs due to their large specific surface area, high electric conductivity, as well as excellent chemical/thermal stability.[8] In general, the pore structure of carbon materials influences the specific capacitance and rate capability through two major aspects: (1) narrow micropores with diameters in the range of the size of the electrolyte ions result in high capacitance because the solvation shell can be partially "stripped off" and the ions experience strong adsorption due to simultaneous electronic interaction with both sides of the pore wall;[9] (2) Additional "transport highways" such as ordered mesopores (i.e., pores of 2-50 nm in size of uniform geometry and orientation) enable rapid diffusion of electrolyte ions onto the inner surface of the porous electrode.[10] These additional transport paths will decrease the volumetric efficiency of the EDLC device but can give rise to outstanding rate capability because the high storage capacity of the micropores can only be utilized under high-power conditions if the ions have rapid access to these adsorption sites.[8a, 11] Thus, to enhance the overall performance of EDLCs, one promising approach is the use of carbon electrode materials with hierarchical pore design combining micropores of appropriate size and ordered mesopores. More relevant than the use in practical devices, such materials are ideal candidates for the investigation of general operating principles and transport mechanisms in EDLCs either by standard electrochemical characterization techniques[10b, 10c] or by more sophisticated methods.[7c, 12] However, there is still a lack of facile approaches to synthesize ordered mesoporous-microporous carbon materials (OMMCs) with controllable size, geometry, ratio, and connectivity of the pores in each single and between the different pore systems.

Typically, OMMCs are accessible via hard-/soft-templating approaches for mesopore formation, followed by subsequent introduction of smaller pores by etching silica co-templates,[13] chemical activation,[14] or metal extraction from mesoporous carbides.[10, 15]

Especially the former methods can result in bottleneck- or torturous pores with broad size distribution, and the size and volume of micropores can hardly be regulated. This limits the high power performance of EDLCs based on such materials and hinders a systematic understanding of the synergistic effects of ordered mesopores and micropores in charge storage. Furthermore, silica etching, chemical activation, or high temperature chlorine treatment of carbides are all dangerous and toxic processes, and a more facile route which minimized use of such tools for synthesizing OMMCs with precise control over the pore structure in both systems over a wide range is still welcomed.

Recently, eutectic salt mixtures composed of $ZnCl_2$ and other chlorides were found to be suitable as templates to develop micro- or small mesopores in carbons. This method is known as salt-templating.[16] Compared to other strategies for generating micropores, such as activation or metal extraction from carbides, salt-templating eliminates the need for harsh conditions either by evaporating salts during carbonization or removing salts with water, which could then be used repeatedly. In consequence, this method is more sustainable, more environmentally-friendly, and potentially favorable to large scale production. Furthermore, the pore size can be regulated by using different salt mixtures (including $LiCl/ZnCl_2$, $NaCl/ZnCl_2$, or $KCl/ZnCl_2$) and by adjusting the component ratios and the amount of salt in relation to the carbon precursor.[16a] However, mesopores generated by salt-templating remain disordered often with a wide size distribution.

To overcome this drawback of salt-templating, a combined synthetic approach towards OMMCs is here put forward, which employs ordered mesoporous silica SBA-15 hard-template and $ZnCl_2$ salt-template as porogens for ordered mesopores and narrow micropores, respectively. Salt- and hard-templates are removed by evaporating salts during carbonization and washing with NaOH solution, respectively. Sucrose is utilized as a renewable carbon precursor with excellent accessibility. Resulting ordered mesoporous hard-salt-templated carbons (OM-HSTCs) offer high specific surface area of more than 2600 $m^2 g^{-1}$ and total pore

volumes exceeding 2.2 $cm^3 g^{-1}$. More importantly, the ratio of micropores to ordered mesopores and their respective sizes can be regulated by adjusting the amount of the salt-template and the type of hard-template. Owing to their high surface area and efficient electrolyte transport in the hierarchical pore system, the OM-HSTCs show high specific capacitance (133 F g^{-1} at 0.1 A g^{-1}) and excellent rate capability (126 F g^{-1} at 40 A g^{-1}) as electrode materials in EDLCs in 1 M tetraethylammonium tetrafluoroborate in acetonitrile ($TEABF_4$/AN) as the electrolyte (cell voltage up to 2.5 V). Accordingly, it achieves high specific energy of 29 Wh kg^{-1} at a specific power of 78 W kg^{-1}, and still maintains 23 Wh kg^{-1} at an ultrahigh specific power of 27 kW kg^{-1} in such organic electrolyte. When operated in 1-ethyl-3-methylimidazolium tetrafluoroborate ($EMImBF_4$) ionic liquid (IL) electrolyte (cell voltage up to 3.5 V), the specific energy reaches up to 59 Wh kg^{-1} with a maximal specific power of 18 kW kg^{-1}. Detailed insights into fundamental structure-performance relationships are achieved by changing the structural parameters and by comparison with purely mesoporous or microporous hard-templates.

2. Results and discussion

OM-HSTC was prepared by employing the SBA-15 hard-template and $ZnCl_2$ salt-template as porogens for ordered mesopores and micropores, respectively **(Scheme 1)**. Aqueous solution containing sucrose as a renewable carbon precursor and $ZnCl_2$ was infiltrated into the mesopores of SBA-15 and the sucrose was polycondensated within the $ZnCl_2$ inside. The salt-template was evaporated during carbonization at 900 °C, leading to the formation of a microporous material (micropore volume 0.17 $cm^3 g^{-1}$) with a notable contribution of mesopores (mesopore volume ~0.26 $cm^3 g^{-1}$) (**Figure S1**). Finally, OM-HSTC was obtained by the removal of the SBA-15. Although a separate step for the removal of the hard-template is still necessary, this synthesis scheme stands out due to the combination of

carbonization and micropore formation by a potentially reusable template without additional activation thus leading to a high yield of carbon from a renewable precursor.

A series of OM-HSTCs (OM-HSTC_1_2.05, OM-HSTC_2_2.05, and OM-HSTC_3_2.05) was prepared by varying the amount of $ZnCl_2$ to explore possible variations of the pore structure. In small-angle X-ray scattering (SAXS) measurements (**Figure 1a**), OM-HTC_0_2.05, OM-HSTC_1_2.05, and OM-HSTC_2_2.05 all show a well-resolved peak assigned to (100) diffractions of the 2-d hexagonal space group (*p6mm*), which locate at $2\theta = 1.08$, 1.04 and 0.96°, respectively. This indicates a larger distance between the centers of the carbon nanorods with increasing amounts of $ZnCl_2$. This is likely because $ZnCl_2$ (until its evaporation) stabilizes the hard-template SBA-15 and provides resistance against shrinkage of during high-temperature treatment, a known effect for sol-gel derived silicas. No diffraction peak at low angle is present for HSTC_3_2.05, suggesting the absence of mesopore ordering because the infiltration solution contains too much of the salt and too little carbon-forming sucrose to stabilize a continuous carbonaceous system. As expected, the purely salt-templated sample STC_2 does not have ordered mesopores, either.

In the Raman spectra (**Figure 1b** and **Figure S2**), the D-band near 1340 cm^{-1} originates from the breathing modes of the six-fold sp^2-hybridized carbon rings in the presence of defects and disorder.[17] The width of the D-band reflects the degree of structural ordering and size distribution of sp^2 rings (i.e., 5-, 6-, 7-, and 8-fold rings). The wide (154-159 cm^{-1} for the OM-HSTCs) D-bands (**Table 1**) in all samples reveal the existence of abundant disordered sections as it is typical for highly microporous carbons.[17a] The G-band near 1580 cm^{-1} is caused by bond stretching of sp^2 carbon in either rings or chains. The peak height ratio of the D- and G-band (I_D/I_G) is proportional to the amount of six-membered sp^2 carbon rings, which is commonly employed to evaluate the level of carbon ordering in porous carbons.[17-18] The I_D/I_G value (**Table 1**) shows a slight rise with the increase of salt-templates (the values of OM-HTC_0_2.05, OM-HSTC_1_2.05, OM-HSTC_2_2.05, and STC_2 equal 1.11, 1.19, 1.24,

and 1.28, respectively). This indicates that adding the salt-template improves the degree of aromatization and thereby the number of six-membered rings at the same carbonization temperature. This, in turn, causes a slightly higher electric conductivity for the OM-HSTCs obtained with a higher amount of $ZnCl_2$.

Thermogravimetric analysis (TGA) of the materials was carried out under air atmosphere (**Figure S3**). OM-HTC_0_2.05 and OM-HSTC_2_2.05 show a quantitative burn off indicating the absence of any residual template in these samples. The other hard-templated carbon samples show a small ash-content (less than 5 wt%) above 600 °C, verifying the nearly complete removal of $ZnCl_2$ and SBA-15 after carbonization and washing with NaOH. At the same time, the presence of traces of inorganic residuals cannot be ruled out for these samples. The onset temperatures of the decomposition of OM-HSTCs is larger than for OM-HTC_0_2.05, which can be ascribed to their higher degree of aromatization as revealed by Raman spectroscopy. The STC_2 carbon obtained by salt-templating without hard-template shows a higher residual mass and therefore the presence of zinc species in this sample, presumably trapped in isolated pores, cannot be ruled out. In case of OM-HSTC_2_2.05, on the contrary, some mesopores are present after carbonization which allow for efficient removal of zinc species from the carbon framework (**Figure S1**). In accordance, the residual zinc in this material detected by electron dispersive x-ray spectroscopy (EDX) after washing is below 1 wt% in both SEM and TEM mode.

N_2 (-196 °C) and CO_2 (0 °C) physisorption experiments were carried out to quantify the OM-HSTCs pore structures (**Figure 2**, **Figure S4**, **Table 1**). OM-HTC_0_2.05, OM-HSTC_1_2.05 and OM-HSTC_2_2.05 exhibit type IV(a) isotherms with a continuous slope above a relative pressure of 0.2, and a narrow hysteresis loop with near-parallel shape in the relative pressure range between 0.4 and 0.9 (**Figure 2a**). These data support the existence of well-defined mesopores in these carbons. To study the transformation of pore structure from OM-HTC_0_2.05 to OM-HSTC_1_2.05 and OM-HSTC_2_2.05, the pore size distribution

(PSD) was further analyzed using the quenched-solid density functional theory (QSDFT) for N_2 adsorbed on carbon with slit/cylindrical pore shape (**Figure 2b**). For all OM-HSTC samples, the amount of micropores (with diameters mainly around 0.9-1.0 nm) is drastically increased after the addition of $ZnCl_2$. Due to its small micropore content (0.11 $cm^3\ g^{-1}$), OM-HTC_0_2.05 has the lowest specific surface area (SSA) of 1263 $m^2\ g^{-1}$, while the larger mesopores contribute only little to the surface area. With increasing the salt loading, SSAs and micropore volumes increase significantly to 2649 $m^2\ g^{-1}$ and 0.53 $cm^3\ g^{-1}$, respectively, in OM-HSTC_2_2.05. OM-HSTC_2_2.05 and STC_2 contain in addition small mesopores with an average diameter of 2.4 nm and 3.2 nm, respectively. These pores likely originate from the percolation of salt-templates and are absent in OM-HSTC_1_2.05 prepared with a lower ratio of $ZnCl_2$/sucrose. The cumulative PSD plots (**Figure 2c**) indicate that the micropores only contribute a small fraction of the total pore volume in the OM-HSTCs. The STC_2 reference shows a type I(b)[19] isotherm, indicating its typical structure containing micropores centered at 0.9 nm with small amount of narrow mesopores. The disordered HSTC_3_2.05 has a high surface area (2131 $m^2\ g^{-1}$) and micropore volume (0.51 $cm^3\ g^{-1}$) but a broader hysteresis loop and a less defined pore size than the OM-HSTCs (**Figure S5**).

The distributions of pores with diameters of 1.5 nm and below have been further quantified by non-local DFT analysis of CO_2 physisorption measurements (**Figure 2d-f**). All samples contain even more narrow micropores with a main diameter of ~0.6 nm in addition to the micropores centered at 0.9-1.0 nm indicated from N_2 physisorption. A smaller $ZnCl_2$/sucrose ratio leads to a larger volume of ultramicropores,[19] that is, pores with diameters of 0.7 nm and below. Hence, OM-HSTC_1_2.05 shows the highest ultramicropore volume among all samples. OM-HSTC_2_2.05 and STC_2 have a higher total micropore volume but smaller ultramicropore volume. This shows that the precise control over the micropore size (a general advantage of salt-templated carbons) is not perturbed by the presence of an additional hard-template.

With the increase of $ZnCl_2$, the average mesopore diameter increases from 4.4 nm (OM-HTC_0_2.05) to 6.6 nm (OM-HSTC_1_2.05) and to 9.9 nm (OM-HSTC_2_2.05) accompanied by a broader distribution. This can be ascribed (in addition to the minimization of shrinking discussed above) to formation of a surface layer of liquid $ZnCl_2$ inside the nanochannels of SBA-15 (**Scheme 2**). The positively charged-Lewis acidic Zn^{2+} ions are prone to interact with the pore walls of the negatively charged, electron lone pair rich SBA-15 during the impregnation step. Therefore, the salt-template distributes partly along the channel and partly inside the carbon precursor into the channels of the silica. This causes the growth of the mesopores between the cylindrical carbon rods after the removal of SBA-15, that is, the mesopore size of the carbon is a sum of the size of the pore walls of SBA-15 and two times the thickness of the salt layer. The precise control of the mesopore sizes can be used to tailor the size of ordered mesopores at a given hard-template and is a unique feature of the salt-templating approach if compared to previously reported synthesis methods for OMMCs.

Scanning electron microscopy (SEM) shows that OM-HTC_0_2.05 (**Figure 3a**) and OM-HSTC samples (**Figure 3c,e**) have the typical particle morphology of hexagonally ordered mesoporous materials like the SBA-15 template. In line with SAXS and physisorption measurements, transmission electron microscopy (TEM) images (**Figure 3b,d,f**) further evidence the ordered mesoporous structure of all hard-templated samples. The mean distances between the carbon rods equal 4.9, 7.6, and 8.8 nm for OM-HTC_0_2.05, OM-HSTC_1_2.05, and OM-HSTC_2_2.05, respectively. This is in good agreement with SAXS and physisorption experiments.

A microporous shell is present around the individual particles in both OM-HSTC_1_2.05 and OM-HSTC_2_2.05 (**Figure 3c,e**), which partly encompasses the ordered carbon rods. OM-HSTC particles thus exhibit a core-shell structure built up by an ordered mesoporous core and a disordered microporous shell. This may be caused by an excess of salt/ precursor mixture surpassing the pore volume of SBA-15 templates. As OM-HTC_0_2.05 without shell

is synthesized with the exact amount of sucrose to fill the pore volume of SBA-15, the mesopores are potentially overfilled with additional $ZnCl_2$. As a result, in the case of OM-HSTCs, a certain amount of the mixed precursor remains outside the SBA-15 particles after impregnation, which turns into the microporous shell after carbonization. Accordingly, further increase of the amount of sucrose in the sample OM-HSTC_2_3 ($ZnCl_2$:sucrose:SBA-15 = 6:3:1 by weight) also leads to an ordered mesoporous core but with a thicker microporous shell (**Figure S6a,b**). OM-HSTC_2_3 is still highly porous with a SSA of 1938 $m^2\ g^{-1}$ and total pore volume of 1.582 $cm^3\ g^{-1}$ (**Figure S6c**) but the higher concentration of sucrose leads to a slight decrease of the porosity and a less well-defined pore size distribution (**Figure S6d**).

In contrast to the ordered materials, STC_2 presents a rather disordered and macroporous morphology without regular geometries (**Figure S7**).

To establish structure-performance relationships of OM-HSTCS for electrochemical energy storage with supercapacitors, the samples were fabricated into electrodes and characterized with cyclic voltammetry (CV) tests, galvanostatic charging/discharging with potential limitation (GCPL), and electrochemical impedance spectroscopy (EIS) in a common organic electrolyte (1 M $TEABF_4$/AN), a typical aqueous electrolyte (1 M Na_2SO_4/H_2O), and solvent-free ionic liquid ($EMImBF_4$).

In $TEABF_4$/AN, OM-HSTCs present rectangle-like CV curves (0-2.5 V) without an obvious distortion even at a scan rate as high as 500 mV s^{-1}, indicating pronouncedly capacitive behavior with a high rate capability (**Figure 4a**, **Figure S8**). The specific capacitance of OM-HSTC_2_2.05 (calculated by GCPL) reaches 133 F g^{-1} at a specific current of 0.1 A g^{-1}, which is 34%, 56%, and 39% higher than that of OM-HSTC_1_2.05 (99 F g^{-1}), OM-HTC_0_2.05 (85 F g^{-1}) and STC_2 (96 F g^{-1}; **Figure 4c**). At a specific current of 40 A g^{-1}, the specific capacitance of OM-HSTC_2_2.05 is still 126 F g^{-1} (about 95% of its initial capacitance). The galvanostatic charging/discharging curves (**Figure 4b**) of OM-HSTCs still show highly symmetry and linear slopes with a small voltage drop of 0.22 V for

OM-HSTC_2_2.05. This excellent rate handling ability suggests a very low resistance in the materials. The voltage drops of OM-HTC_0_2.05 and STC_2 are much higher: 0.80 V at 40 A g^{-1} and 1.41 V at 25 A g^{-1}, respectively, indicating in both cases surface polarization and thereby contact resistance effects.

Cycling stability tests were performed by charging and discharging (0-2.5 V) at a specific current of 20 A g^{-1} for 10,000 cycles followed by holding the cell voltage of 2.5 V for 100 h (interrupted by cycling at 20 A g^{-1} after every 10 h). OM-HSTC_2_2.05 shows excellent stability with 86% capacitance retention, after continued cycling and voltage holding (**Figure 4d**).

The carbon samples show comparable EDLC performance when tested in 1 M Na_2SO_4/H_2O neutral aqueous electrolyte (**Figure 5**, **Figure S9**). CV curves of OM-HSTC_2_2.05 (**Figure 5a**) exhibit a rectangular shape and GPCL measurements show a specific capacitance of 125 F g^{-1} at 0.1 A g^{-1} (**Figure 5c**), considerably exceeding that of OM-HSTC_1_2.05 (95 F g^{-1}), OM-HTC_0_2.05 (77 F g^{-1}) and STC_2 (78 F g^{-1}). At an ultrahigh specific current of 40 A g^{-1}, the specific capacitance of OM-HSTC_2_2.05 still reaches 117 F g^{-1}. The corresponding GCPL curves are highly symmetric triangle with only a small voltage drop of 0.17 V at 40 A g^{-1} (**Figure 5b**). In contrast, OM-HTC_0_2.05 shows a moderate rate capability (67% capacitance remaining), and the purely microporous STC_2 presents the lowest performance (**Figure 5b,c**).

The EDLC performance shows that the OM-HSTCs provide not only higher specific capacitance, but also a rate capability which is superior to that of OM-HTC_0_2.05. The observed excellent capacitance of OM-HSTCs could be attributed to their high specific surface area and micropore volume (**Table 1**) which offers many active sites for ion adsorption with optimum size to distort solvation shells and provide close approach of the ions to the pore walls. The increase of salt-templates further enhances these two positive

factors by increasing the size of ordered mesopores and the micropore volume, leading to the higher capacitance and rate capability of OM-HSTC_2_2.05 compared to OM-HSTC_1_2.05.

To further understand the difference of rate capabilities between the carbon samples, EIS was employed to characterize the impedance behaviors of EDLCs based on different carbon electrode materials (**Figure 6a,c**). The frequency responses in organic and aqueous electrolytes (**Figure 6b,d**) confirm the excellent rate capability of OM-HSTCs. The capacitances of OM-HSTCs show saturation in organic and aqueous electrolytes at a frequency around ~0.3 Hz, suggesting that near-equilibrium ion adsorption could be achieved within several seconds, much faster than that in OM-HTC_0_2.05 and STC_2. Quantified by the frequency f_0 at which the capacitance drops to the half of its maximum value, OM-HSTC_2_2.05 and OM-HSTC_1_2.05 display fast frequency responses with f_0 of 0.85 Hz and 0.73 Hz in organic electrolyte, significantly surpassing that of OM-HTC_0_2.05 (0.46 Hz) and STC_2 (0.14 Hz), indicating the faster charge/discharge rate of hierarchical OM-HSTCs. The frequency responses in the aqueous electrolyte show the same trend. The f_0 of OM-HSTC_2_2.05, OM-HSTC_1_2.05, OM-HTC_0_2.05, and STC_2 equals 0.85 Hz, 0.74 Hz, 0.55 Hz, and 0.21 Hz, respectively. The nearly vertical curves in the low-frequency region of the Nyquist plots in organic (**Figure 6a**) and aqueous electrolytes (**Figure 6c**) demonstrate the near-ideal capacitive behavior of all EDLCs. By extrapolating the vertical portion of the curves to the real axis, the equivalent series resistance (R_{ESR}) in organic electrolyte is obtained to be 1.53 Ω cm^{-2} and 1.57 Ω cm^{-2} (1.20 Ω cm^{-2}, and 1.38 Ω cm^{-2} in aqueous electrolyte) for OM-HSTC_2_2.05, and OM-HSTC_1_2.05, respectively. In both electrolytes, this is much lower than that for OM-HTC_0_2.05 and STC_2 and consistent with the low voltage drops of OM-HSTCs in GCPL measurements. In the middle-frequency region, the 45° sloped curve known as the Warburg portion is related to the transport of electrolyte ions into the carbon pores. Compared with STC_2, the very short Warburg lengths (related to the transport of electrolyte ions into the carbon pores) observed for the OM-HSTCs electrodes

suggest their low resistance for ion transport due to the rapid diffusion facilitated by the ordered mesopores. Moreover, the thin microporous shells of the OM-HSTCs (**Figure 6b,c)** provide a short diffusion distance for ions to rapidly reach the surface of its inner micropores, while the defects on the shells enable the superb mobility of the ion flux between the ordered mesoporous cores and the outside electrolyte. In the high frequency region, the intercept along the real axis reveals the intrinsic resistances (R_s) of electrode material, electrolyte, current collector, as well as the contact resistances between them. In comparison with OM-HTC_0_2.05, OM-HSTCs present smaller R_s, suggesting the lowest electronic resistance in the electrode material. Considering the similar ordered mesoporous core in OM-HTC_0_2.05 and OM-HSTCs, it can be concluded that the difference in the carbon aromatization by $ZnCl_2$ catalysis is crucial to reduce the electronic resistance in the electrodes.

The mesoporous cores composed of carbon rods in OM-HTC_0_2.05 and OM-HSTCs differ in sizes, amount of micropores inside, and degree of carbon aromatization. For the sake of excluding these effects, OM-HSTC without a shell (OM-HSTC_1_1.31) was prepared and compared with OM-HSTC_1_2.05. OM-HSTC_1_1.31 was synthesized by regulating the amount of sucrose and $ZnCl_2$ according to the pore volume of SBA-15 while keeping the same ratio of sucrose to $ZnCl_2$ as in OM-HSTC_1_2.05. In this manner, the micro-/mesoporous cores of OM-HSTC_1_1.31 are comparable in structure to that of OM-HSTC_1_2.05, that is, the effects of the microporous shell are highlighted by the comparison of their EDLC performance (**Figure 7** and **Figure S10**). The SEM images of OM-HSTC_1_2.05 (**Figure 7a,c**) clearly show a shell around the particles which is absent in OM-HSTC_1_1.31 (**Figures 7b,d**). The processing of the as-made powders into EDLC electrodes shows the presence of few smaller particles with sheet-like morphology originating from broken OM-HSTC particles and the fiber-like binder web but the general morphology of OM-HSTC powder particles can be maintained in the EDLC electrodes. Both samples present the same ordered mesoporous cores as shown by SAXS (**Figure 7e**) and TEM images (**Figure 3d**,

Figure S11). From the N_2 and CO_2 physisorption measurements (**Figure 7f** and **Figure S12**) we see that the major difference between the samples is the larger amount of mesopores in OM-HSTC_1_1.31 than in OM-HSTC_1_2.05 (**Table 1**). This is reasonable because the micro-/mesoporous core of OM-HSTC_1_2.05 coexists with the purely microporous shell, whereas OM-HSTC_1_1.31 only contains the core in which the mesopores are located. While the mesopores are similar in size and the SSA is comparable in both samples, a minor difference is the higher amount of micropores in OM-HSTC_1_2.05 because of the microporous shells.

The CV curves of OM-HSTC_1_1.31- and OM-HSTC_1_2.05-based EDLCs in organic electrolyte (**Figure 7g,h**) show typical quasi-rectangular shapes. But for OM-HSTC_1_1.31 without shells, the shape at 500 mV s^{-1} becomes significantly more elliptical as compared to OM-HSTC_1_2.05 indicating the lower rate capability of the former. In the GCPL curves (**Figure 7i**), the voltage drop at 40 A g^{-1} of OM-HSTC_1_1.31 (0.89 V) is more than two times that of OM-HSTC_1_2.05 (0.42 V). According to that, the OM-HSTC_1_2.05 with shell shows lower polarization and thus higher capacitance retention under high power conditions in both CV and GCPL tests (**Figure 7g,h,i**). The differences caused by the presence of a microporous shell in the particles are further underlined by EIS (**Figure 7j**). The microporous shell around the carbon particles of OM-HSTC_1_2.05 apparently reduces the internal resistance of the EDLCs by facilitating transfer of charged species between the carbon particles into the electrodes.

Finally, the ionic liquid (IL) $EMImBF_4$ with a wide voltage window of 0-3.5 V was employed as the electrolyte to test the EDLC performance of OM-HSTC_2_2.05 (**Figure 8**). Since the energy capacity of an EDLC is proportional to the square of its operating voltage, ionic liquids (at similar capacity) are promising to address the main problem of current EDLCs, their low energy density.[20] Also here, CV curves show a nearly rectangular shape at different scan rates (5-200 mV s^{-1}), GCPL curves are nearly symmetrical with small voltage

drops at high current densities (0.64 V at 10 A g^{-1}), and the curves in the low-frequency region of Nyquist plots are nearly vertical (**Figures 8a-c**). In the CV curves, an increase of the cathodic current at 3.0-3.5 V and a small peak at around 2.0 V (disappeared when increasing the scan rate over 50 mV s^{-1}) may be associated with either trace amounts of water in the ionic liquid or the reaction of the electrolyte with the oxygen-containing functional groups on the carbon surface, leading to some deviation from the ideal capacitor-like behavior.[21] Owing to such side-effects, a high specific capacitance of 138 F g^{-1} is obtained from the GCPL curve (**Figure 8b**) at 0.1 A g^{-1} in the IL electrolyte (0-3.5 V). Because the capacitance (which corresponds to the charge divided by the voltage) is still in the same range as for the aqueous and organic electrolytes but the voltage is significantly higher, this value also shows that more charge must be stored in the electrodes of IL-based electrolytes.

The gravimetric and volumetric Ragone plots (**Figure 9**) of EDLCs using OM-HSTC_2_2.05 as electrodes show that the symmetric cells provide the highest specific energy of 29 Wh kg^{-1} at a specific power of 78 W kg^{-1}, and still maintain 23 Wh kg^{-1} at a specific power of 27 kW kg^{-1} in $TEABF_4$/AN electrolyte. In the ionic liquid electrolyte, the specific energy reaches 59 Wh kg^{-1} at a specific power of 1 kW kg^{-1}, and maintains 25 Wh kg^{-1} when the specific power increases to 18 kW kg^{-1}. The comparison with other advanced porous carbon materials that can be found in the literature[6, 7g, 7h, 9e] confirms its high performance (**Figure 9a**). This property is attributed to the high content of micropores for ion storage and the ordered mesopores for fast charge transfer, as well as the thin microporous shell for reduced electric resistance. Yet, the low density of the highly mesoporous OM-HSTC electrodes (~0.3 g cm^{-3}) leads to a moderate energy density (<10 Wh L^{-1} and < 20 Wh L^{-1} in organic and IL electrolyte, respectively).

3. Conclusions and outlook

Ordered mesoporous carbon with high content of micropores can be synthesized by a novel combined hard/salt-templating method. Large specific surface area up to 2649 $m^2 g^{-1}$ and high pore volume exceeding 2.2 $cm^3 g^{-1}$ are obtained when applying optimized synthetic conditions. The synergic effects of the large amount of micropores, highly ordered mesopores, and a thin microporous shell endow abundant active sites for charge storage, efficient electrolyte transport, and improved electrical conductivity, resulting in the superior EDLC performance. EDLCs based on OM-HSTC electrodes achieve high specific capacitance (133 F g^{-1} in organic electrolyte and 138 F g^{-1} in ionic liquid electrolyte at 0.1 A g^{-1}) as well as excellent rate capability (126 F g^{-1} at 40 A g^{-1} in organic electrolyte, and 103 F g^{-1} at 20 A g^{-1} in ionic liquid electrolyte) combined with admirable stability. Accordingly, it provides high specific energy of 29 Wh kg^{-1} at a specific power of 78 W kg^{-1}, and still maintains 23 Wh kg^{-1} at a high specific power of 27 kW kg^{-1} in organic electrolyte. When using an ionic liquid, the specific energy is up to 59 Wh kg^{-1} with a maximal specific power of 18 kW kg^{-1}.

We see the major benefit of the novel OM-HSTC materials as model substances for fundamental investigations on EDLC operating mechanisms (e.g., with NMR spectroscopy[7c-f] or SAXS/SANS[7b, 22]) because the synthesis procedure allows adjustment of the pore sizes/geometries and ratios between the pore systems over a wide range and independent from each other. This feature remains difficult to be achieved with established methods towards OMMCs and other nanoporous carbons. Finally, the possibility of depositing a microporous shell around a hierarchical carbon particle will open new possibilities for applications where the encapsulation of guest species into a porous matrix is required.[23]

4. Experimental Section

Synthesis of OM-HSTCs and reference carbons: For the synthesis of OM-HSTCs, ordered mesoporous silica (SBA-15, hydrothermally treated at 130 °C) and $ZnCl_2$ were employed as hard- and salt template, respectively. In a typical procedure, 1.0 g SBA-15 was first

impregnated with 4 mL of an aqueous solution of 1.25 g sucrose, 2.5 g $ZnCl_2$, and 0.14 g concentrated sulfuric acid in a petri dish. The mixture was then heated to 100 °C and held for 6 h followed by subsequent heating to 160°C for another 6 h under air to polymerize of the carbohydrate molecules. Afterwards, the mixture was impregnated again with 3 mL of an aqueous solution of 0.8 g sucrose, 0.8 g $ZnCl_2$, and 0.09 g concentrated sulfuric acid, followed by repeated heating to 100 °C for 6 h and 160 °C for 6 h. The polymerized carbohydrate was carbonized and the salt template was removed in a horizontal tubular furnace at 900°C for 2 h under N_2 flow. The heating ramp was set to be 60°C h^{-1} from room temperature to 300°C and 150°C h^{-1} from 300 °C to 900 °C. SBA-15 was removed by heating the carbon/silica composite in 5 M NaOH aqueous solution overnight under reflux followed by filtration, washing with large amounts of water, and drying at 60 °C. The final product was named as OM-HSTC_X_Y, where X and Y represent the mass ratio of $ZnCl_2$/sucrose and sucrose/SBA-15, respectively (for example, OM-HSTC_2_2.05 for the above sample). Other hard-salt templated carbons, including OM-HSTC_1_2.05, HSTC_3_2.05, OM-HSTC_1_1.31, and OM-HSTC_2_3, were synthesized by the same method but with different amounts of $ZnCl_2$ and sucrose (**Table S1**). Hard-templated ordered mesoporous carbon CMK-3 (herein referred to as OM-HTC_0_2.05) and salt-templated microporous carbon (STC_2) were employed as reference samples. OM-HTC_0_2.05 was synthesized by the similar procedure as OM-HSTC_2_2.05 without the addition of salt templates. STC_2 was prepared by the salt-template method. Typically, 5 mL aqueous solution of 2 g sucrose, 4 g $ZnCl_2$ and 0.2 g concentrated sulfuric acid was dried at 100°C for 6 h, before being heated to 160 °C and kept for 6 h. The mixture was then transferred to a horizontal tubular furnace for carbonization at 900 °C for 2 h under N_2 flow (150°C h^{-1} heating rate).

Material characterization: N_2 physisorption experiments were carried out at -196 °C on a Quadrasorb apparatus (40-60 mg sample) and an Autosorb IQ instrument (10-20 mg sample for low-pressure measurements), both from Quantachrome Instruments. Prior to all

measurements, the samples were outgassed at 150 °C for 20 h under vacuum. SSAs were calculated using the multi-point Brunauer-Emmett-Teller (BET) model (p/p_0 = 0.05-0.2). Total pore volumes (V_t) were determined at p/p_0 = 0.95. SSAs and V_t were calculated from the data obtained by measurements with 40-60 mg sample. Pore size distributions were calculated using the quenched-solid density functional theory (QSDFT) method (adsorption branch kernel) for N_2 adsorbed on carbon with a slit/cylindrical pore shape at -196 °C from the data obtained by the low-pressure measurements. CO_2 physisorption experiments were carried out at 0 °C on the Autosorb instrument to investigate the pores with the diameter smaller than 1.5 nm. Corresponding PSDs were calculated by the non-local density functional theory (NLDFT) method for CO_2 adsorbed on carbon at 0 °C.

Further structural characterization was carried out by scanning electron microscopy (SEM, LEO 1550-Gemini) operating at 3 kV and high-resolution transmission electron microscopy (TEM, JEOL ARM 200F) operating at 200 kV. To prepare the TEM samples, carbon particles were dispersed in ethanol, followed by dropping several droplets on a carbon-coated copper TEM grid and drying at room temperature. SAXS was conducted with a Bruker AXS with $CuK_{\alpha 1}$ radiation (0.154 nm). Raman spectra were recorded using a Renishaw inVia Raman Microscope operating with an objective (Nikon, 10x/0.25, ∞/- WD 6.1) and an excitation wavelength of 532 nm with a power of 4.0 mW. After the background noise was subtracted from the obtained Raman spectra, the D, D^2, A, and G bands were fitted with a Lorentz function. Thermogravimetric analysis (TGA) was conducted with a Netzsch TG 209 F1 device under constant artificial air flow in platinum pans at a heating rate of 10°C min^{-1} to 1000 °C.

Fabrication of EDLCs and electrochemical measurements: To prepare free-standing electrodes for EDLCs, carbon materials and polytetrafluoroethylene (PTFE, 60 wt% solution in H_2O from Sigma Aldrich) were mixed with a mass ratio of ~9:1 in ethanol. The solution was then transferred to a glass plate and mixed with razor blades until it changed to a rubber-

like consistency. Then it was placed into aluminum foil and rolled to uniformly thin sheets (thicknesses 180±10 µm) using a commercial roll mill, followed by punching into free-standing electrode disks of 10 mm in diameter. The areal density of an electrode was about 4 mg cm^{-2}. The electrodes were dried at 120°C for 12 h under vacuum. EDLCs were tested with a symmetrical two-electrode configuration employing three different electrolytes, namely 1 M Na_2SO_4 aqueous solution, 1 M tetraethylammonium tetrafluoroborate/acetonitrile solution, and 1-ethyl-3-methylimidazolium tetrafluoroborate (≥99.0%, Sigma Aldrich). Typically, a custom-built cell (with a spring to control the pressure at 10 MPa and highly conductive titanium pistons)[24] was assembled using a pair of circular electrodes sandwiching a separator, with 100 µL electrolyte and two platinum foils as current collectors. Commercially available Dreamweaver Silver (Dreamweaver International Inc.) separator of 13 mm in diameter was used for aqueous and $EMImBF_4$ electrolyte, while a 25 µm trilayer polypropylene-polyethylene-polypropylene membrane (Celgard 2325, 13 mm in diameter) was used as separator in $TEABF_4$/AN electrolyte. For the aqueous electrolyte, the device assembly took place under air atmosphere. For the other two electrolytes, EDLCs were assembled in an argon filled glove box (H_2O < 0.1 ppm, O_2 < 0.1 ppm). A Biologic MPG-2 galvanostat/potentiostat was used for electrochemical characterization. All measurements were performed at room temperature. The electrochemical impedance spectroscopy was performed at open circuit potential with a sinusoidal signal over a frequency range from 20 kHz to 10^{-2} Hz at an amplitude of 10 mV. The specific gravimetric capacitance of a single electrode C_{EIS} (F g^{-1}), was calculated according to the following formula and normalized according to the specific gravimetric capacitance at 10^{-2} Hz:

$$C_{EIS} = \frac{2|Im(Z)|}{2\pi f[(Im(Z))^2+(Re(Z))^2]\cdot m} \quad (1)$$

where f is the operating frequency (Hz), $Im(Z)$, and $Re(Z)$ are the imaginary and real component of the total device impedance (Ω), and m is the active mass in a single carbon electrode (g).

Cyclic voltammetry (CV) tests were performed at scan rates of 2-500 mV s^{-1}. The carbon differential gravimetric capacitance for CV plots, C_d (F g^{-1}), and the integral gravimetric capacitance, C (F g^{-1}), were calculated according to the following equations:

$$C_d = \frac{2I}{m\gamma} \tag{2}$$

$$C = (\int_{V_1}^{V_2} I_+(V)dV - \int_{V_1}^{V_2} I_-(V)dV)/m \cdot \gamma \cdot (V_2 - V_1) \tag{3}$$

where I is the current (A), γ is the scan rate (V s^{-1}), and m is the active mass in a single carbon electrode (g).

Galvanostatic charge/discharge with potential limitation (GCPL) was applied at specific currents between 0.1 and 40 A g^{-1} in different cell voltage ranges (-0.5 V to +0.5 V, 0 to +2.5 V, and 0 to +3.5 V for aqueous, organic and ionic liquid electrolytes, respectively). The carbon gravimetric capacitance, C (F g^{-1}), was calculated according to the following equation:

$$C = \frac{2Q_{dis}}{(V - V_{drop})m} \tag{4}$$

Where Q_{dis} (C) is the charge of the discharging cycle, V (V) is the discharging potential change, V_{drop} (V) is the voltage drop at the beginning of the discharge, and m (g) is the active mass in a single carbon electrode.

The specific energy, E (Wh kg^{-1}) and specific power, P (W kg^{-1}) of EDLCs were estimated via:

$$E = \frac{1}{8\times3.6} C(V - V_{drop})^2 \tag{5}$$

$$P = \frac{E\times3600}{\Delta t} \tag{6}$$

where V (V) is the discharging potential change, V_{drop} (V) is the voltage drop at the beginning of the discharge, Δt (s) is the discharging time.

The energy density, E_V (Wh L^{-1}) and power density, P_V (W L^{-1}) of EDLCs were calculated by:

$$E_V = \rho \times E \quad (7)$$

$$P_V = \rho \times P \quad (8)$$

where ρ (g cm^{-3}) is the density of carbon electrodes, E (Wh kg^{-1}) and P (W kg^{-1}) are the specific energy and the specific power of carbon electrodes, respectively.

For long-term stability tests in organic electrolyte, the cells were charged and discharged by galvanostatic cycling for 10,000 cycles. Afterwards, the voltage was kept at 2.5 V for 100 h, and the specific capacity was measured every 10 h by galvanostatic cycling at 20 A g^{-1}.

Supporting Information

Supporting Information is available from the Wiley Online Library or from the author.

Acknowledgements

R.Y. acknowledges Changzhou T-Linder Spiral Bevel Gear Co., Ltd. For financial support. V.P. kindly thanks Prof. Eduard Arzt for his continuing support. M.O. and R.W. acknowledge financial support by the German Chemical Industry Fund.

References

[1] a) J. Liu, J.-G. Zhang, Z. Yang, J. P. Lemmon, C. Imhoff, G. L. Graff, L. Li, J. Hu, C. Wang, J. Xiao, G. Xia, V. V. Viswanathan, S. Baskaran, V. Sprenkle, X. Li, Y. Shao, B. Schwenzer, *Adv. Funct. Mater.* **2013**, *23*, 929; b) B. C. Melot, J. M. Tarascon, *Acc. Chem. Res.* **2013**, *46*, 1226; c) H. Wang, Y. Yang, L. Guo, *Adv. Energy Mater.* **2017**, *7*, 1601709; d) D. Larcher, J. M. Tarascon, *Nat. Chem.* **2015**, *7*, 19.

[2] a) G. Wang, L. Zhang, J. Zhang, *Chem. Soc. Rev.* **2012**, *41*, 797; b) J. Yan, Q. Wang, T. Wei, Z. Fan, *Adv. Energy Mater.* **2014**, *4*, 1300816; c) P. Simon, Y. Gogotsi, *Acc. Chem. Res.* **2013**, *46*, 1094; d) P. Simon, Y. Gogotsi, *Nat. Mater.* **2008**, *7*, 845; e) F. Beguin, V. Presser, A. Balducci, E. Frackowiak, *Adv. Mater.* **2014**, *26*, 2219.

[3] R. Kotz, M. Carlen, *Electrochim. Acta* **2000**, *45*, 2483.

[4] a) J. R. Miller, P. Simon, *Science* **2008**, *321*, 651; b) W. Gu, G. Yushin, *WIREs. Energy Environ.* **2014**, *3*, 424.

[5] a) H. Zhang, G. Cao, Y. Yang, Z. Gu, *Carbon* **2008**, *46*, 30; b) Y. Korenblit, A. Kajdos, W. C. West, M. C. Smart, E. J. Brandon, A. Kvit, J. Jagiello, G. Yushin, *Adv. Funct. Mater.* **2012**, *22*, 1655.

[6] X. M. Zhang, Y. Q. Jiao, L. Sun, L. Wang, A. P. Wu, H. J. Yan, M. C. Meng, C. G. Tian, B. J. Jiang, H. G. Fu, *Nanoscale* **2016**, *8*, 2418.

[7] a) C. Merlet, B. Rotenberg, P. A. Madden, P. L. Taberna, P. Simon, Y. Gogotsi, M. Salanne, *Nat. Mater.* **2012**, *11*, 306; b) C. Prehal, C. Koczwara, N. Jäckel, A. Schreiber, M. Burian, H. Amenitsch, M. A. Hartmann, V. Presser, O. Paris, *Nat. Energy* **2017**, *2*, 16215; c) L. Borchardt, M. Oschatz, S. Paasch, S. Kaskel, E. Brunner, *Phys. Chem. Chem. Phys.* **2013**, *15*, 15177; d) Alexander C. Forse, John M. Griffin, C. Merlet, J. Carretero-Gonzalez, A.-Rahman O. Raji, Nicole M. Trease, Clare P. Grey, *Nat. Energy* **2017**, *2*, 16216; e) A. C. Forse, J. M. Griffin, H. Wang, N. M. Trease, V. Presser, Y. Gogotsi, P. Simon, C. P. Grey, *Phys. Chem. Chem. Phys.* **2013**, *15*, 7722; f) M. Deschamps, E. Gilbert, P. Azais, E. Raymundo-Pinero, M. R. Ammar, P. Simon, D. Massiot, F. Beguin, *Nat. Mater.* **2013**, *12*, 351; g) J. J. Xu, F. Xu, M. Qian, F. F. Xu, Z. L. Hong, F. Q. Huang, *Adv. Mater.* **2017**, *29*, 1701674; h) Z. Chen, B. Deng, K. Du, X. Mao, H. Zhu, W. Xiao, D. Wang, *Adv. Sustainable Syst.* **2017**; i) S. Leyva-Garcia, D. Lozano-Castello, E. Morallon, D. Cazorla-Amoros, *J. Mater. Chem. A* **2016**, *4*, 4570; j) P. P. Yu, Z. M. Zhang, L. X. Zheng, F. Teng, L. F. Hu, X. S. Fang, *Adv. Energy Mater.* **2016**, *6*, 1601111.

[8] a) L. Borchardt, M. Oschatz, S. Kaskel, *Mater. Horiz.* **2014**, *1*, 157; b) T. Chen, L. Dai, *Mater. Today* **2013**, *16*, 272; c) E. Frackowiak, Q. Abbas, F. Béguin, *J. Energ. Chem.* **2013**, *22*, 226; d) H. Jiang, P. S. Lee, C. Li, *Energy Environ. Sci.* **2013**, *6*, 41; e) Q. Wang, J. Yan, Z. Fan, *Energy Environ. Sci.* **2016**, *9*, 729; f) Y. Zhai, Y. Dou, D. Zhao, P. F. Fulvio, R. T. Mayes, S. Dai, *Adv. Mater.* **2011**, *23*, 4828.

[9] a) J. Chmiola, C. Largeot, P. L. Taberna, P. Simon, Y. Gogotsi, *Angew. Chem. Int. Ed. Engl.* **2008**, *47*, 3392; b) J. Chmiola, G. Yushin, Y. Gogotsi, C. Portet, P. Simon, P. L. Taberna, *Science* **2006**, *313*, 1760; c) N. Jäckel, P. Simon, Y. Gogotsi, V. Presser, *ACS Energy Letters* **2016**, *1*, 1262; d) E. Raymundo-Piñero, K. Kierzek, J. Machnikowski, F. Béguin, *Carbon* **2006**, *44*, 2498; e) M. Sevilla, A. B. Fuertes, *ACS Nano* **2014**, *8*, 5069.

[10] a) H.-J. Liu, J. Wang, C.-X. Wang, Y.-Y. Xia, *Adv. Energy Mater.* **2011**, *1*, 1101; b) M. Rose, Y. Korenblit, E. Kockrick, L. Borchardt, M. Oschatz, S. Kaskel, G. Yushin, *Small* **2011**, *7*, 1108; c) M. Oschatz, E. Kockrick, M. Rose, L. Borchardt, N. Klein, I. Senkovska, T. Freudenberg, Y. Korenblit, G. Yushin, S. Kaskel, *Carbon* **2010**, *48*, 3987.

[11] Z. Yu, L. Tetard, L. Zhai, J. Thomas, *Energy Environ. Sci.* **2015**, *8*, 702.

[12] C. Koczwara, S. Rumswinkel, C. Prehal, N. Jackel, M. S. Elsasser, H. Amenitsch, V. Presser, N. Husing, O. Paris, *ACS Appl. Mater. Interfaces* **2017**, *9*, 23319.

[13] R. Liu, Y. Shi, Y. Wan, Y. Meng, F. Zhang, D. Gu, Z. Chen, B. Tu, D. Zhao, *J. Am. Chem. Soc.* **2006**, *128*, 11652.

[14] a) J. Jin, S. Tanaka, Y. Egashira, N. Nishiyama, *Carbon* **2010**, *48*, 1985; b) Y. Lv, F. Zhang, Y. Dou, Y. Zhai, J. Wang, H. Liu, Y. Xia, B. Tu, D. Zhao, *J. Mater. Chem.* **2012**, *22*, 93; c) J. Wang, S. Kaskel, *J. Mater. Chem.* **2012**, *22*, 23710.

[15] M. Oschatz, L. Borchardt, K. Pinkert, S. Thieme, M. R. Lohe, C. Hoffmann, M. Benusch, F. M. Wisser, C. Ziegler, L. Giebeler, M. H. Rümmeli, J. Eckert, A. Eychmüller, S. Kaskel, *Adv. Energy Mater.* **2014**, *4*, 1300645.

[16] a) N. Fechler, T. P. Fellinger, M. Antonietti, *Adv. Mater.* **2013**, *25*, 75; b) S. Porada, F. Schipper, M. Aslan, M. Antonietti, V. Presser, T. P. Fellinger, *ChemSusChem* **2015**, *8*, 1867.

[17] a) M. Oschatz, P. Pré, S. Dörfler, W. Nickel, P. Beaunier, J.-N. Rouzaud, C. Fischer, E. Brunner, S. Kaskel, *Carbon* **2016**, *105*, 314; b) S. Osswald, J. Chmiola, Y. Gogotsi, *Carbon* **2012**, *50*, 4880.

[18] M. Pawlyta, J.-N. Rouzaud, S. Duber, *Carbon* **2015**, *84*, 479.

[19] M. Thommes, K. Kaneko, A. V. Neimark, J. P. Olivier, F. Rodriguez-Reinoso, J. Rouquerol, K. S. W. Sing, *Pure Appl. Chem.* **2015**, *87*, 1051.

[20] a) A. A. Kornyshev, *J. Phys. Chem. B* **2007**, *111*, 5545; b) M. Salanne, *Top. Curr. Chem.* **2017**, *375*, 63.
[21] a) L. Wei, M. Sevilla, A. B. Fuertes, R. Mokaya, G. Yushin, *Adv. Funct. Mater.* **2012**, *22*, 827; b) A. Vu, X. Li, J. Phillips, A. Han, W. H. Smyrl, P. Bühlmann, A. Stein, *Chem. Mater.* **2013**, *25*, 4137.
[22] S. Boukhalfa, L. He, Y. B. Melnichenko, G. Yushin, *Angew. Chem. Int. Ed. Engl.* **2013**, *52*, 4618.
[23] a) Z. Li, Y. Jiang, L. X. Yuan, Z. Q. Yi, C. Wu, Y. Liu, P. Strasser, Y. H. Huang, *ACS Nano* **2014**, *8*, 9295; b) F. Schüth, *Chem. Mater.* **2014**, *26*, 423.
[24] D. Weingarth, M. Zeiger, N. Jäckel, M. Aslan, G. Feng, V. Presser, *Adv. Energy Mater.* **2014**, *4*, 1400316.

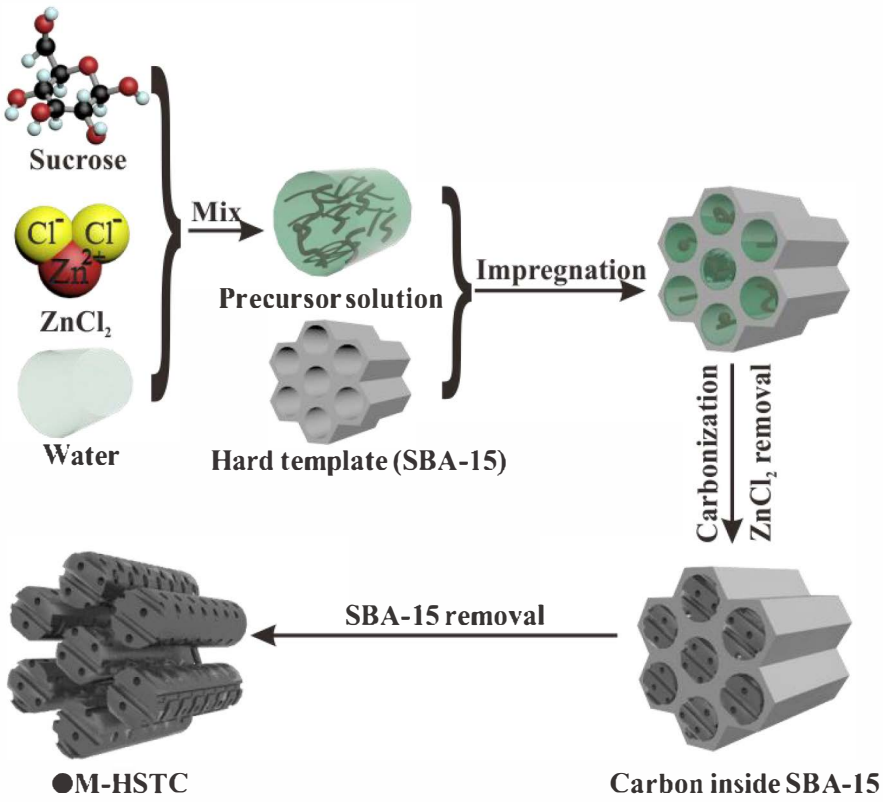

Scheme 1. Preparation of ordered mesoporous hard-salt-templated carbon (OM-HSTC).

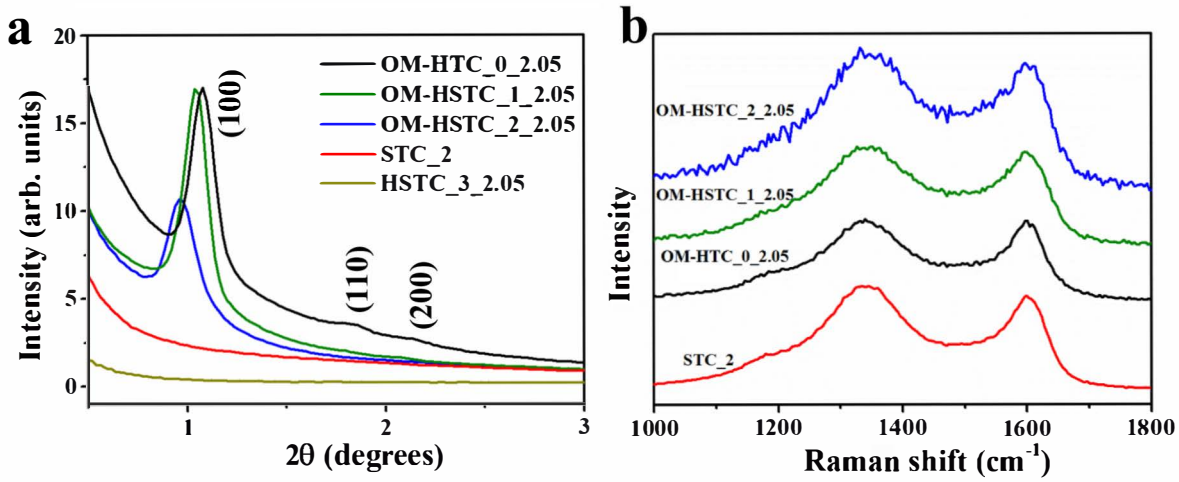

Figure 1. (a) SAXS patterns and (b) Raman spectra of OM-HSTCs and the OM-HTC_0_2.05/STC_2 references.

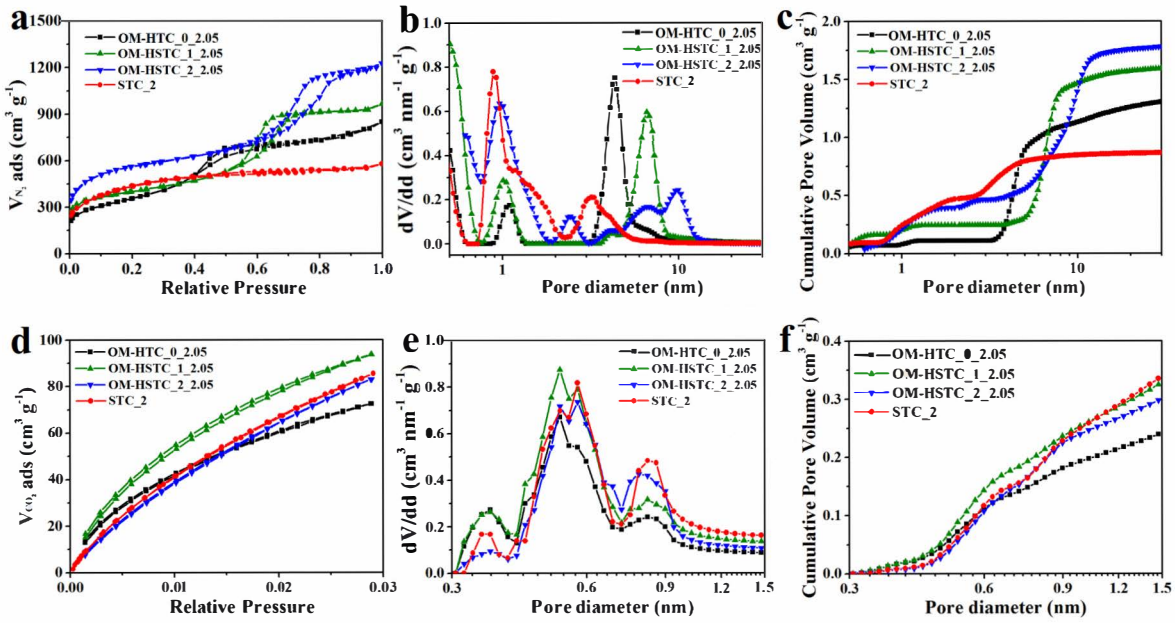

Figure 2. (a) N_2 physisorption (at -196 °C) isotherms with corresponding (b) differential and (c) cumulative QSDFT PSDs as well as (d) CO_2 physisorption (at 0 °C) isotherms with corresponding (e) differential and (f) cumulative NLDFT PSDs of OM-HSTCs and the OM-HTC_0_2.05/STC_2 references.

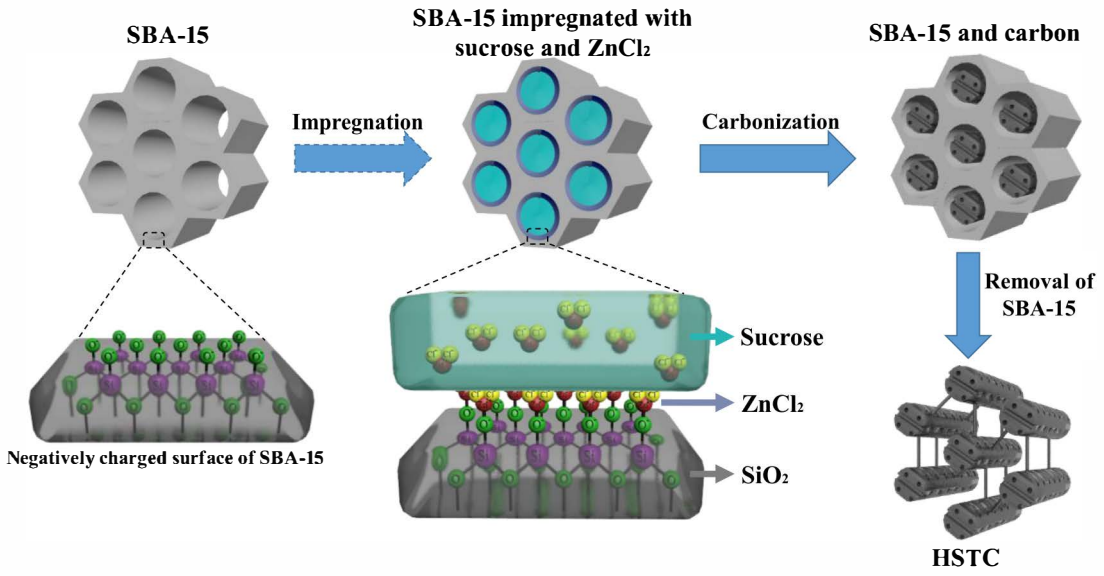

Scheme 2. Possible mechanism of enlargement of mesopore size caused by salt templating.

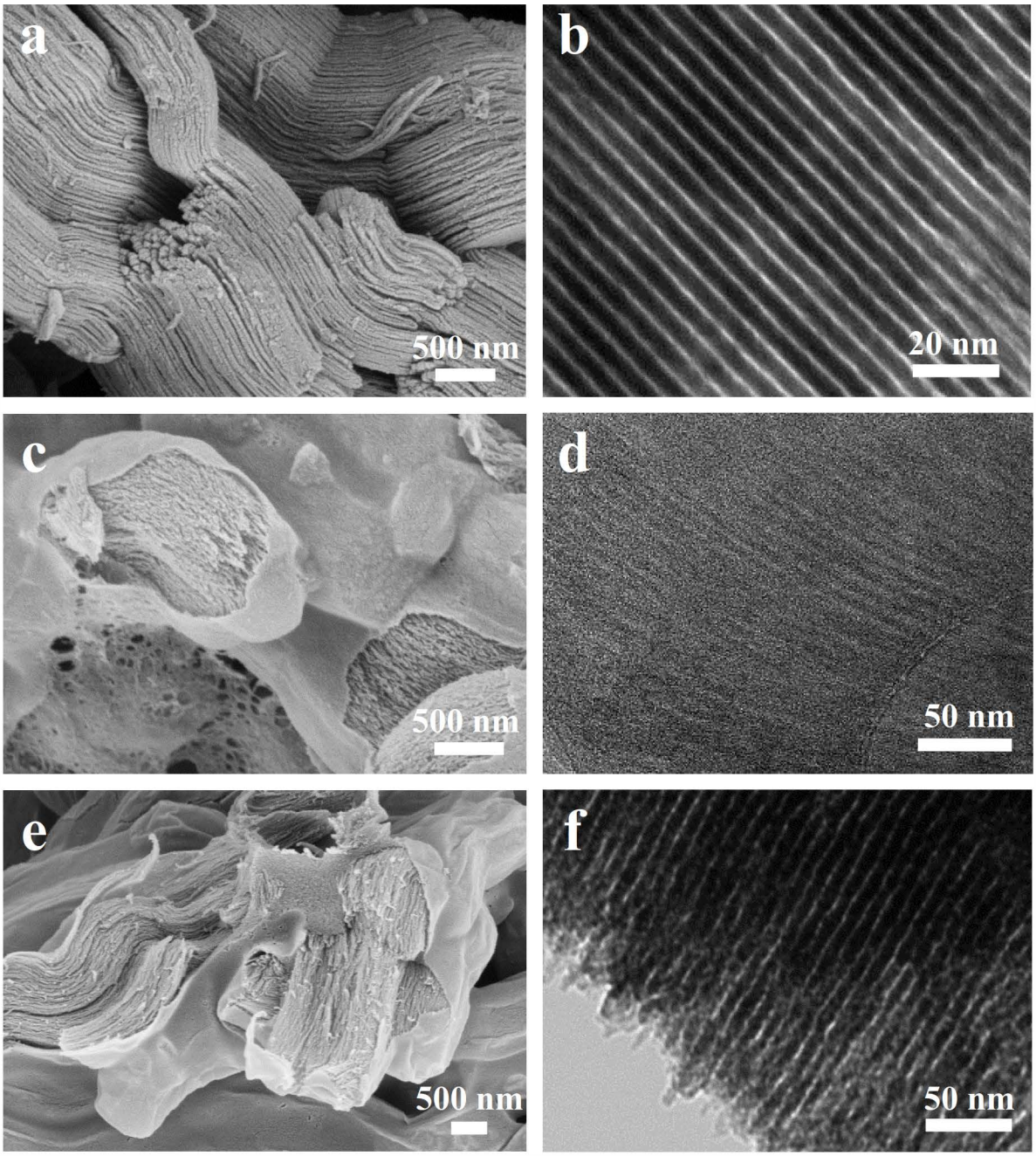

Figure 3. SEM and TEM images of (a, b) OM-HTC_0_2.05, (c, d) OM-HSTC_1_2.05, (e, f) OM-HSTC_2_2.05.

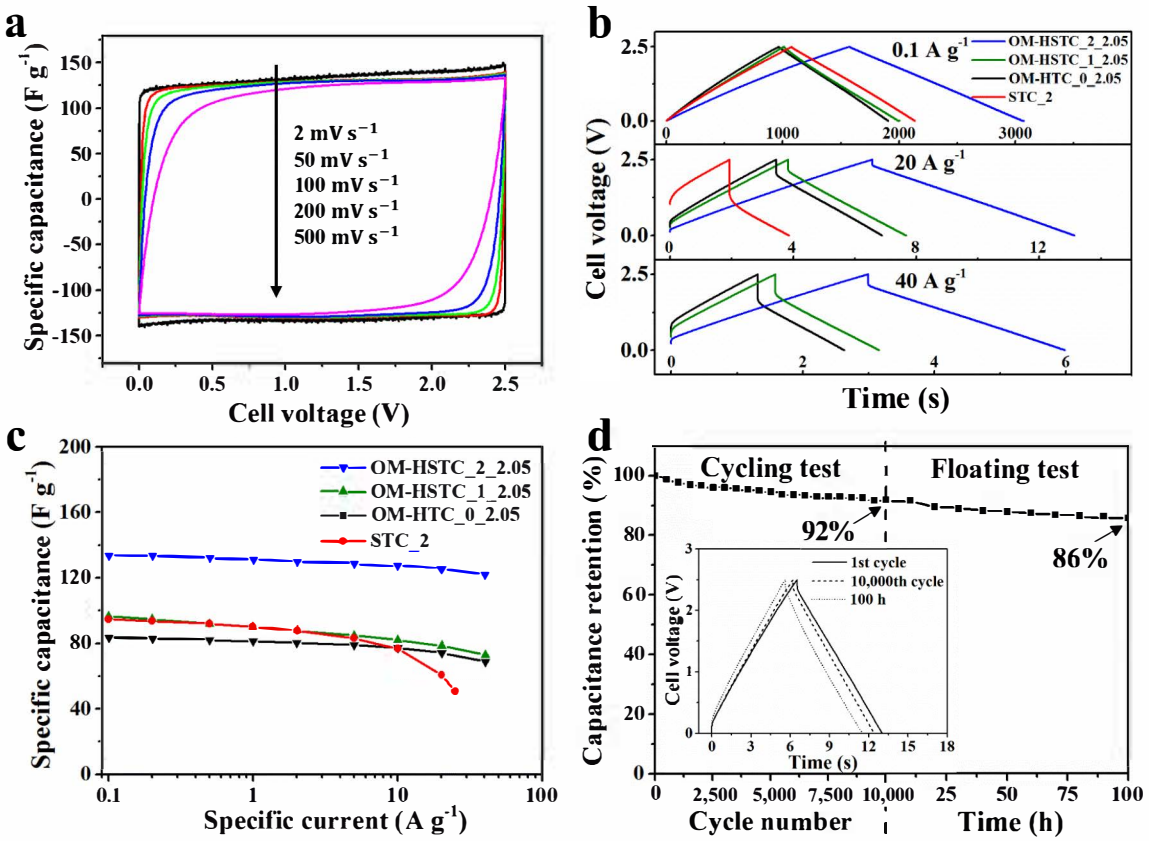

Figure 4. (a) Cyclic voltammograms of OM-HSTC_2_2.05 at different scan rates, (b) charge/discharge profiles at different current densities, (c) capacitance retention of different carbon materials with current density increase, and (d) cycle and floating stability of OM-HSTC_2_2.05 at a specific current of 20 A g^{-1} for 10,000 cycles and 100 h floating at 2.5 V. The inset in (d) shows the charge/discharge profiles of the initial test, after the 10,000th cycling test, and after 100 h floating test. All measurements were conducted in 1 M $TEABF_4$/AN as electrolyte.

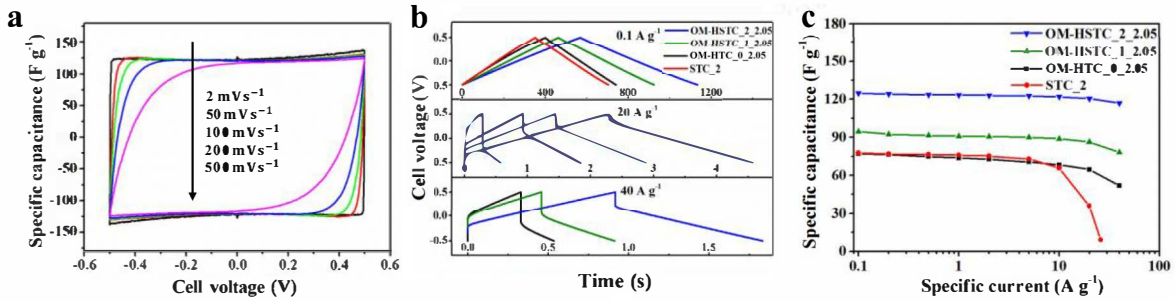

Figure 5. (a) Cyclic voltammograms of OM-HSTC_2_2.05 at different scan rates, (b) charge/discharge profiles at different specific currents, and (c) capacitance retention of different carbon materials with current density increase. All measurements were conducted in 1 M Na_2SO_4/H_2O electrolyte.

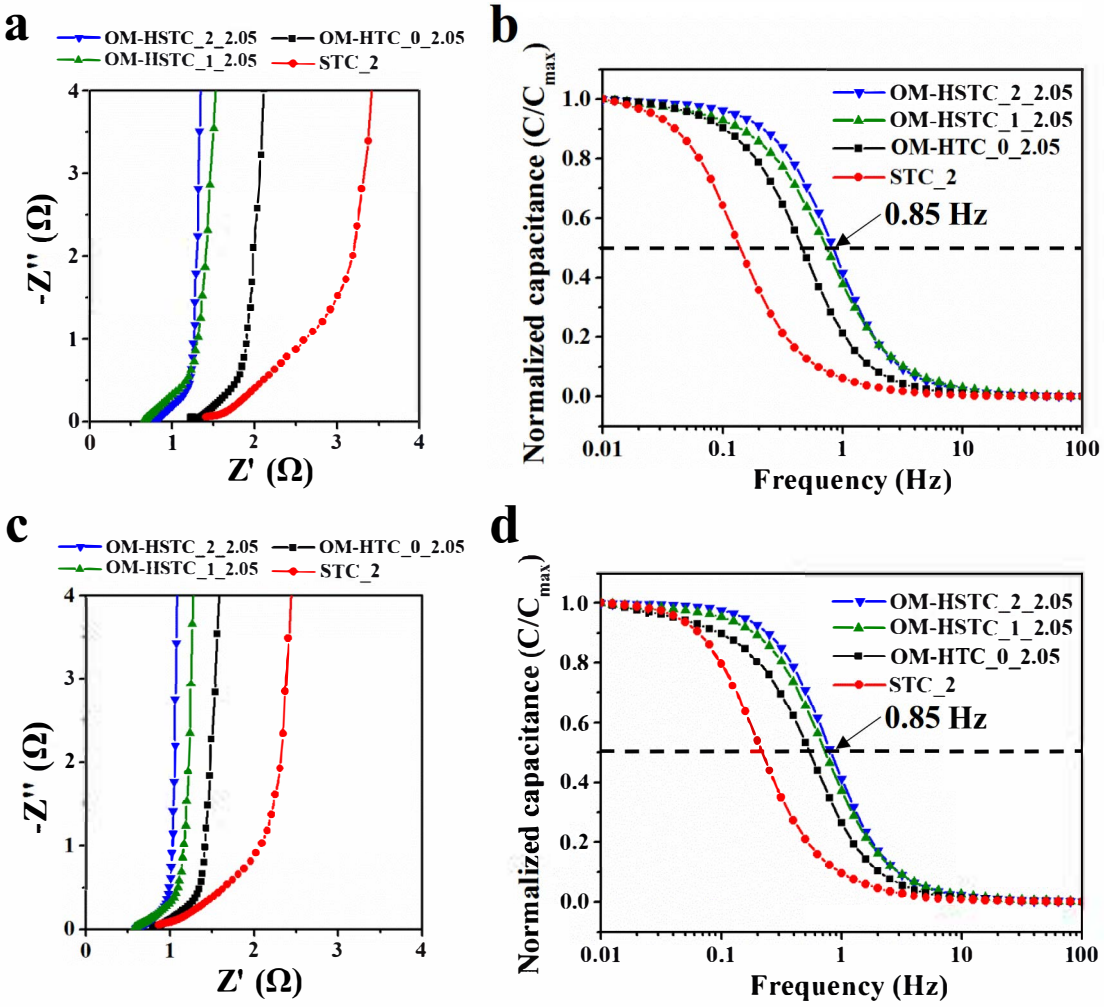

Figure 6. Nyquist plots and frequency responses of different carbon materials tested in (a, b) 1 M $TEABF_4/AN$, (c, d) 1 M Na_2SO_4/H_2O.

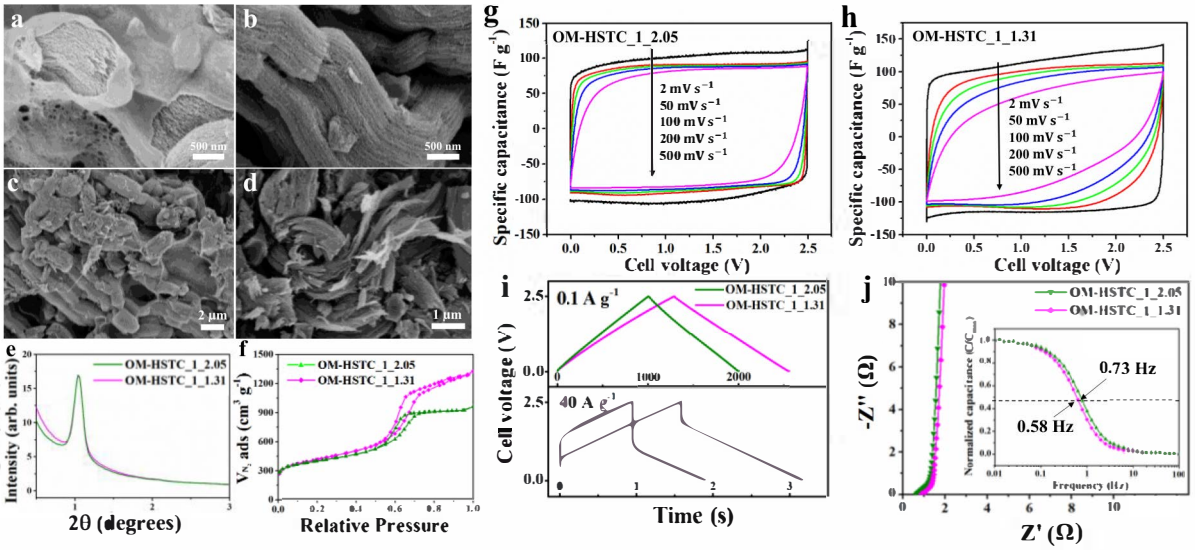

Figure 7. (a, b) SEM images of OM-HSTC_1_2.05 and OM-HSTC_1_1.31. (c, d) SEM images of electrodes prepared from OM-HSTC_1_2.05 and OM-HSTC_1_1.31. (e) SAXS patterns, (f) N_2 physisorption (-196 °C) isotherms, (g, h) Cyclic voltammograms, (i) charge/discharge profiles at different specific currents, and (j) Nyquist plots of OM-HSTC_1_2.05 and OM-HSTC_1_1.31. The inset in (j) shows frequency responses. All measurements were conducted in 1 M $TEABF_4$/AN.

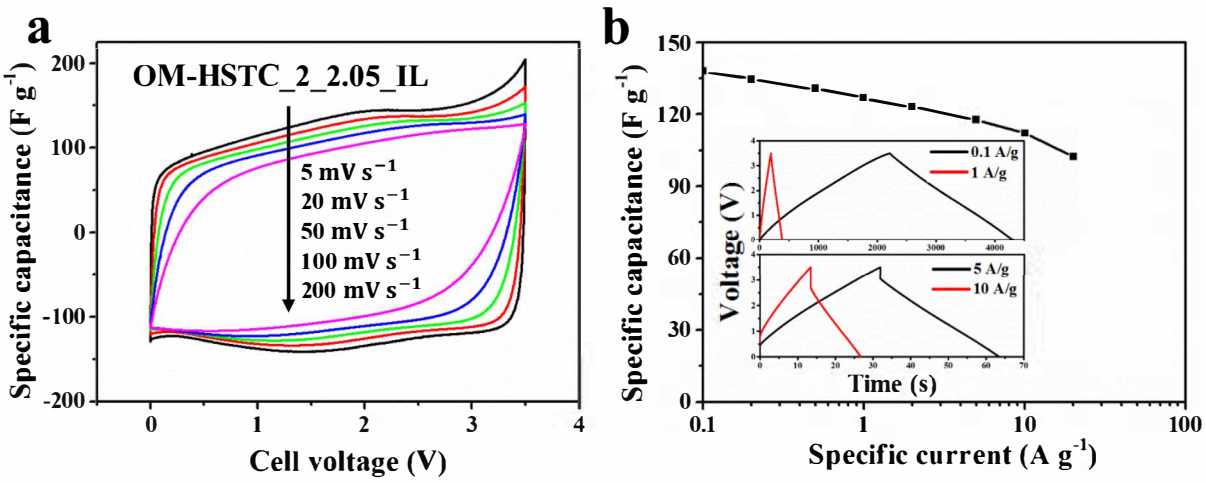

Figure 8. EDLC performance of OM-HSTC_2_2.05 tested in the ionic liquid electrolyte of $EMImBF_4$. (a) Cyclic voltammograms at different scan rates, (b) capacitance retention of different carbon electrodes with current density increase. The inset in (b) shows the charge/discharge voltage profile at different specific currents).

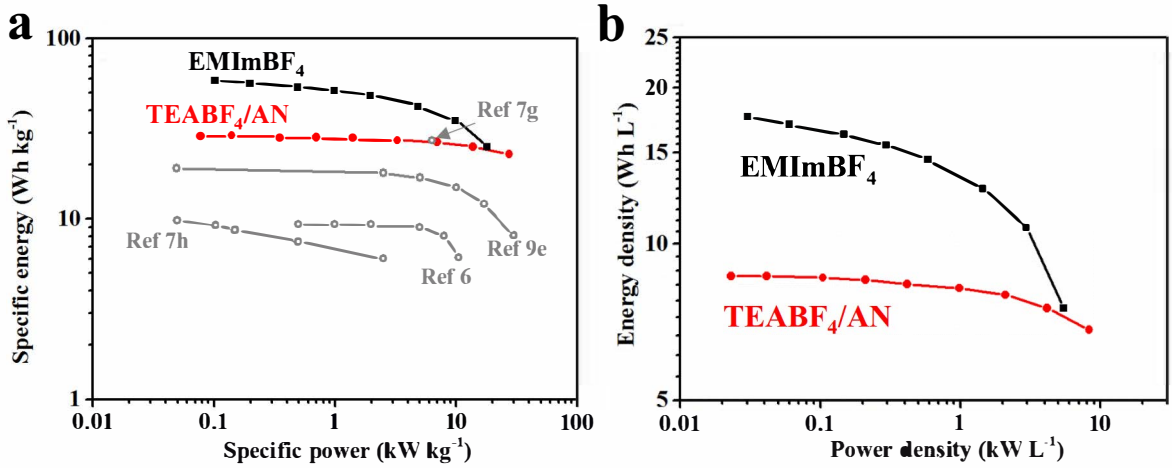

Figure 9. Gravimetric and volumetric Ragone plots of EDLCs using OM-HSTC_2_2.05 as electrodes.

Table 1. Specific surface area (SSA), total pore volume (V_t), micropore volume (V_{mic}), and ultramicropore volume ($V_{ultramicro}$, calculated from CO_2 physisorption), I_D/I_G ratio, and FWHM of the D-band of the carbon materials obtained by Raman spectroscopy and N_2 physisorption at -196 °C.

Sample	SSA ($m^2\ g^{-1}$)	V_t ($cm^3\ g^{-1}$)	V_{mic} ($cm^3\ g^{-1}$)	$V_{ultramicro}$ ($cm^3\ g^{-1}$)	I_D/I_G	FWHM of D band (cm^{-1})
OM-HSTC_2_2.05	2649	2.22	0.53	0.15	1.24	154
OM-HSTC_1_2.05	1439	1.43	0.24	0.18	1.19	159
OM-HSTC_1_1.31	1460	1.99	0.16	0.18	1.19	158
HSTC_3_2.05	2131	1.80	0.51	n.d.	1.27	194
OM-HTC_0_2.05	1263	1.26	0.11	0.14	1.11	158
STC_2	1557	0.85	0.47	0.15	1.28	161